

Metal Oxide/Graphene/Metal Sandwich Structure for Efficient Photoelectrochemical Water Oxidation

Guancai Xie, Beidou Guo, and Jian Ru Gong*

Single-layer graphene (SLG) has drawn considerable interest in photoelectrochemical (PEC) cells due to its atomically flat pinhole-free structure and remarkable in-plane carrier mobility. It is challenging, however, to obtain efficient SLG-modified photoelectrodes for PEC water splitting mainly due to the inefficient charge transfer interface. Here, a transition metal oxide/SLG/transition metal sandwich structure modified n-Si-based model photoanode is constructed to regulate the interfacial charge transfer behavior for enhanced PEC water oxidation performance. In this sandwich configuration, SLG tailors the morphology, structure, and work function properties of surface metal electrocatalysts to obtain both higher thermodynamic photovoltage and faster kinetical charge transfer at the semiconductor/electrolyte interface. In addition, SLG promotes the surface catalytic reaction as an effective charge trap and storage layer. This study provides a new structural design to engineer the SLG interfacial properties for high-performance energy conversion devices.

1. Introduction

Graphene derivatives, such as graphene oxide and reduced graphene oxide, have aroused increasing interest in the photoelectrochemical (PEC) water-splitting system, by virtue of their thin and robust structures and significant properties, for example, high transmittance, large surface area, and facile chemical modification.^[1] Either as an electron mediator to accelerate charge separation and transport^[1d,e,2] or a catalytic layer to offer more catalytic reaction centers,^[3] graphene derivatives have boosted the PEC water-splitting performance. However, their electronic properties are subject to various structural features, including doping, defects, functional groups and so on.^[4] Also, the reduction degree of reduced graphene oxide has a considerable influence on the activity.^[5] Lack of homogeneity of structure and properties and accordingly clear understanding

of the fundamentals has cast doubt on the controllability of graphene derivatives for PEC water splitting.

By contrast, single-layer graphene (SLG) can be prepared in a controllable manner with a low level of structural defects using chemical vapor deposition.^[6] Moreover, SLG has larger carrier mobility, higher conductivity, lower light absorption, and better chemical stability compared with its derivatives.^[7] In addition, the pinhole-free large-area SLG film can be transferred onto arbitrary substrates and protect semiconductor photoelectrodes from degradation.^[8] These remarkable physicochemical properties of SLG promise crucial improvement in the PEC water-splitting performance.

In previous studies, SLG has been mostly utilized as the atom/ion diffusion

barrier with the aim of preventing the corrosion of semiconductors or avoiding atomically intermixing between semiconductors and electrocatalysts.^[8,9] What's more, SLG has been reported as a surface modification layer to improve the surface photo-hole injection of semiconductors by suppressing surface traps or reinforcing hole extraction,^[10] or as a buried Schottky junction component to provide the water-splitting photovoltage.^[9a,c] Despite progress that has been made, SLG-modified photoanodes typically render a poor PEC water-splitting performance as a result of their small photovoltage and slow surface reaction kinetics caused by the low work function and inferior catalytic activity of SLG, respectively. Given the unique merits of SLG in the PEC water-splitting system, rational design of the SLG interfacial structure is central to taking full advantage of this material for high-performance energy conversion devices.

Herein, we propose a sandwich structure to modify the n-Si photoanode in a form of transition metal oxide/SLG/transition metal for enhanced PEC oxygen evolution reaction (OER). Si is chosen as a model semiconductor in the experiment because of its low bandgap, high carrier mobility, easy availability, economic affordability, well-established processing techniques, and environment and human friendliness.^[11] This sandwich configuration boosts several definite advantages with respect to obtaining high PEC OER performance: 1) the transition metal oxide layer with a high work function, e.g. 5.2–5.6 eV for NiO_x,^[12] introduced between the n-Si and SLG with a low work function of ≈4.4 eV^[13] can obtain a larger photovoltage; 2) the transition metal modified on the SLG surface can become an efficient OER electrocatalyst owing to the large surface area and support effect of SLG;^[14] and 3) the SLG interlayer with high

G. Xie, B. Guo, J. R. Gong
CAS Key Laboratory for Nanosystem and Hierarchical Fabrication
National Center for Nanoscience and Technology
Chinese Academy of Sciences (CAS) Center for Excellence in Nanoscience
Beijing 100190, China
E-mail: gongjr@nanoctr.cn
J. R. Gong
University of CAS
Beijing 100049, China

 The ORCID identification number(s) for the author(s) of this article can be found under <https://doi.org/10.1002/adfm.202210420>.

DOI: 10.1002/adfm.202210420

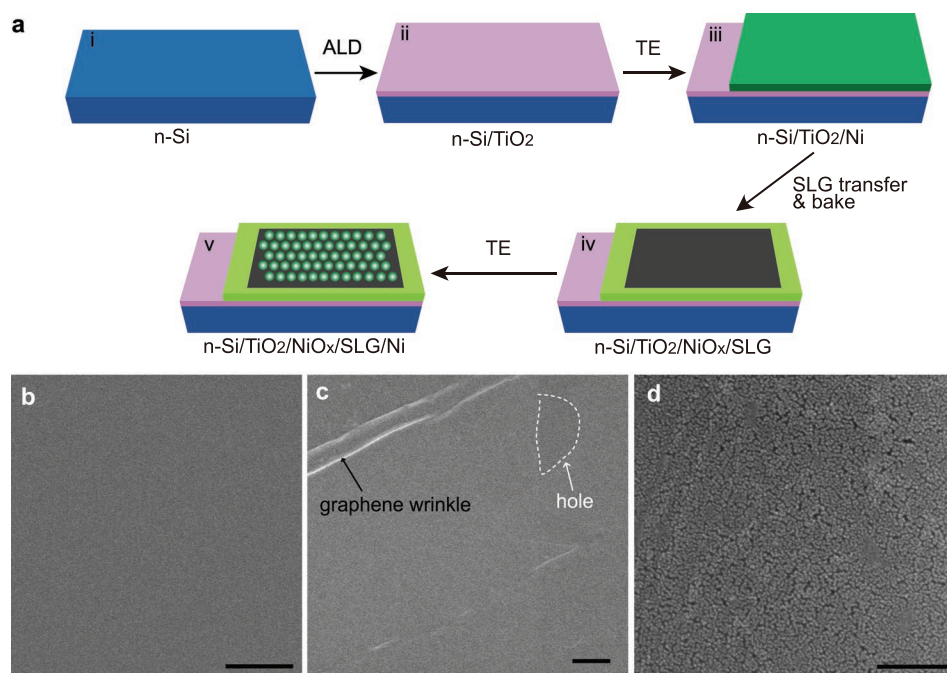


Figure 1. a) Schematic procedure for the photoanode preparation with 5 steps. ALD and TE represent for atomic layer deposition and thermal evaporation, respectively. And SEM images of the representative $n\text{-Si}/\text{TiO}_2/\text{NiO}_x/\text{SLG}/\text{Ni}$ photoanode for the step iii b), iv c), and v d). Scale bars, 200 nm.

conductivity and carrier mobility has potential to engineer the interfacial charge transfer. In view of the exceptional features of this design, the synergistic regulation of the hole photocurrents was realized. Furthermore, SLG in the sandwich structure can not only tailor the morphology, structure, and work function of the surface catalyst for tuning photovoltage and interfacial charge transfer, but also act as an effective charge trap and storage layer for advancing surface catalytic reaction. This study sheds light on the significance of engineering the SLG interlayer for its wide applications, not least in the solar energy conversion field.

2. Results and Discussion

In this work, the $n\text{-Si}$ -based photoanodes modified with transition metal oxide/SLG/transition metal ($\text{MO}_x/\text{SLG}/\text{M}$, $\text{M} = \text{Ni}$, Co , and Fe) sandwich structures were investigated. Taking the $n\text{-Si}/\text{TiO}_2/\text{NiO}_x/\text{SLG}/\text{Ni}$ as an example, the fabrication procedure is schematically illustrated in **Figure 1a**. First, a ≈ 2 nm thin layer of TiO_2 was deposited on the $n\text{-Si}$ substrate by atomic layer deposition (ALD) as a tunnel dielectric to passivate the Si high surface states that spell Fermi level pinning and low OER activities.^[12,15] Then a metallic Ni film was thermally evaporated on the TiO_2 surface, forming a compact and flat surface (Figure 1b). Subsequently, a SLG monolayer sheet was transferred onto the Ni layer surface using a poly(methyl methacrylate) (PMMA)-assisted wet-transfer method and graphene wrinkle can be observed in the SEM image (Figure 1c). During this process, the thin Ni layer was transformed into a NiO_x film resulting from the thermal oxidation of Ni in the air.^[16] Noted that it might be difficult to completely cover the

NiO_x layer with the SLG sheet due to the possible damage to SLG in the transfer operation, as shown by the occasionally spotted hole in the SLG sheet. Finally, the Ni upper layer was thermally evaporated on the SLG surface. The typical thickness of both Ni layers is 2 nm, which is optimized for the OER activity. As shown in Figure 1d, the Ni outer layer on the SLG sheet forms a uniform nanoisland film, whereas the Ni film in the SLG-free $n\text{-Si}/\text{TiO}_2/\text{NiO}_x/\text{Ni}$ control sample is flat and compact (Figure S1, Supporting Information), implying the SLG sheet plays a key role in forming the Ni nanoislands. The formation of Ni nanoislands on SLG is due to the small ratio between adsorption energy of Ni adatoms on SLG and the bulk binding energy of Ni, indicating the Volmer–Weber growth mode of Ni.^[17] Compared to the $n\text{-Si}/\text{TiO}_2/\text{NiO}_x/\text{Ni}$ with the flat Ni film, the photoanode with the Ni nanoisland structure is beneficial to the PEC OER activity on two counts. One reason is that the $n\text{-Si}/\text{TiO}_2/\text{NiO}_x/\text{SLG}/\text{Ni}$ can absorb more light for additional light scattering on the surface, as evidenced by the light transmittance and reflectance spectra in Figure S2 (Supporting Information), and the other is that the photoanode can obtain a larger photovoltage because the ion-permeable nature of the nanoisland film is prone to forming a higher barrier height.^[18]

The surface chemical compositions of the $n\text{-Si}/\text{TiO}_2/\text{NiO}_x/\text{SLG}/\text{Ni}$ photoanode were analyzed by X-ray photoelectron spectroscopy (XPS). To avoid the interference from the outer Ni layer on the inner NiO_x , the $n\text{-Si}/\text{TiO}_2/\text{NiO}_x/\text{SLG}$ sample was also tested as a reference. **Figure 2a,b** shows the high-resolution XPS spectra of Ni 2p before and after deposition of the outer Ni layer, both of which show two spin-orbit doublets of Ni 2p_{3/2} and Ni 2p_{1/2} along with their shakeup satellites. For the $n\text{-Si}/\text{TiO}_2/\text{NiO}_x/\text{SLG}$ sample, the Ni 2p_{3/2} peaks can be further deconvolved by two peaks centered at 855.9 and 857.1 eV,

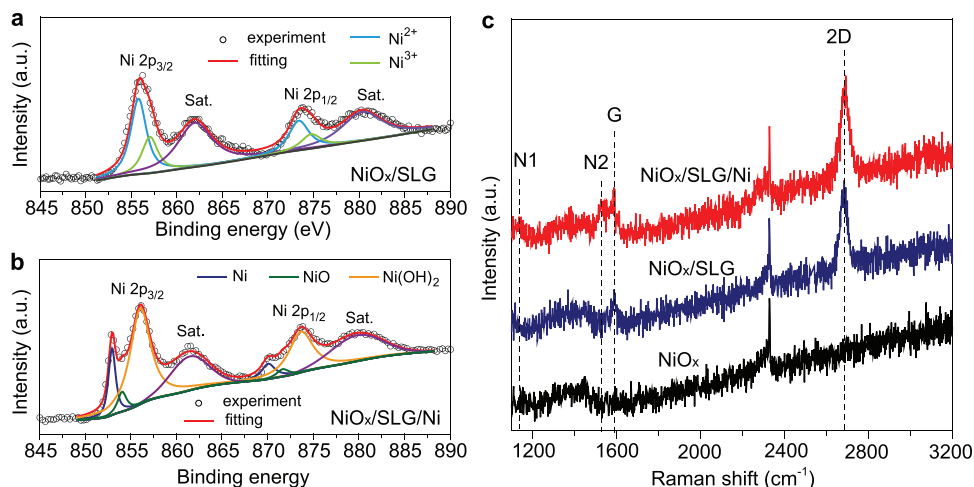


Figure 2. High-resolution XPS spectra of Ni 2p for a) the n-Si/TiO₂/NiO_x/SLG and b) n-Si/TiO₂/NiO_x/SLG/Ni photoanodes. c) Raman spectra of the n-Si/TiO₂/NiO_x/SLG/Ni, n-Si/TiO₂/NiO_x/SLG, and n-Si/TiO₂/NiO_x photoanodes, denoted as NiO_x/SLG/Ni, NiO_x/SLG, and NiO_x respectively for clarity in the figures here and hereafter unless otherwise specified.

which are separated with their corresponding Ni 2p_{1/2} peaks by a binding energy difference of 176 and 178 eV, respectively. The above XPS features clearly indicate the coexistence of Ni²⁺ and Ni³⁺ oxidation states in the n-Si/TiO₂/NiO_x/SLG sample, proving oxidation of the inner Ni to NiO_x.^[19] After deposition of the outer Ni layer, the n-Si/TiO₂/NiO_x/SLG/Ni exhibits three main peaks of Ni 2p_{3/2} at 852.7, 853.4, and 856.0 eV, and three main peaks of Ni 2p_{1/2} centered at 869.8, 870.9, and 873.7 eV, which can be assigned to metallic Ni, NiO, and Ni(OH)₂, respectively.^[12] The presence of NiO and Ni(OH)₂ on the photoanode surface is due to the spontaneous oxidation of Ni at ambient conditions and/or from the inner NiO_x layer.^[20] The other two SLG-free control samples n-Si/TiO₂/NiO_x and n-Si/TiO₂/NiO_x/Ni display the same deconvolution peaks in their Ni 2p XPS spectra as the n-Si/TiO₂/NiO_x/SLG and n-Si/TiO₂/NiO_x/SLG/Ni, respectively (Figure S3, Supporting Information), indicating that insertion of SLG does not change chemical compositions of both the inner NiO_x and outer Ni layers.

Raman spectroscopy was then conducted to investigate the structure property of the n-Si/TiO₂/NiO_x/SLG/Ni photoanode. The SLG used in our experiment is confirmed to be monolayer graphene with low defects (Figure S4, Supporting Information), and the appearance of the G and 2D peaks in the n-Si/TiO₂/NiO_x/SLG proves the presence of SLG on the NiO_x layer (Figure 2c).^[21] Interestingly, two new Raman peaks appear at ≈1140 cm⁻¹ denoted as N1 and ≈1528 cm⁻¹ designated as N2 for the n-Si/TiO₂/NiO_x/SLG/Ni, compared to those of the n-Si/TiO₂/NiO_x and n-Si/TiO₂/NiO_x/SLG samples. The new peaks can be more clearly observed by preparation of the same NiO_x/SLG/Ni structure on the SiO₂ substrate, owing to the higher signal-to-noise ratio of SLG on the SiO₂ relative to that on the Si (Figure S4, Supporting Information). It suggests that some Ni grains of the outer Ni layer could chemisorb on the SLG by forming the (111) crystal orientation in the growth process of the Ni nanoislands, and have a higher work function than those with other stable facets.^[22] The favorable formation of the Ni (111) crystal orientation in the n-Si/TiO₂/NiO_x/SLG/Ni photoanode can be further verified from its higher work func-

tion as compared to that in the SLG-free n-Si/TiO₂/NiO_x/Ni photoanode (Figure S5, Supporting Information). Therefore, the SLG interfacial layer can also engineer the work function of the surface material, besides tailor the morphology and crystal structure of the material deposited on it.

The PEC OER activity of the photoanodes was evaluated by performing linear sweep voltammetry measurements in 1 M KOH solution under simulated solar irradiation without correction for resistance losses in the electrolyte solution. The thickness of both the NiO_x and Ni layers was optimized to be 2 nm in the n-Si/TiO₂/NiO_x/SLG/Ni photoanode for the activity test (Figure S6, Supporting Information), and this parameter was used in the following samples. The measured current density–potential (*J*–*V*) curves in **Figure 3a** clearly display that the n-Si/TiO₂/NiO_x/SLG/Ni photoanode totally outperforms the SLG-free n-Si/TiO₂/NiO_x/Ni control in all figures of merits, showing the SLG interlayer is indispensable. In further comparison with the n-Si/TiO₂/NiO_x/Ni/SLG and n-Si/TiO₂/SLG/NiO_x/Ni, the other two reference photoanodes with the SLG as the top and bottom layer in the sandwich structure, respectively, even lag far behind the worse SLG-free control, revealing that only the sandwich configuration with the SLG as the interlayer functions well. The lower PEC OER activity of the two reference photoanodes with the SLG as the top and bottom layer in the sandwich structure could be attributed to the limitation of mass-transfer process through the SLG cover and the low work function of the SLG, respectively.^[23] The n-Si/TiO₂/NiO_x/SLG/Ni photoanode achieves a low photocurrent onset potential (potential at 1 mA cm⁻²) of 1.03 ± 0.01 V versus the reversible hydrogen electrode (*V*_{RHE}), a saturated current density of 34.7 ± 1.21 mA cm⁻², and a photocurrent of 21.1 ± 0.96 mA cm⁻² at 1.23 *V*_{RHE} which is higher than those of the reported Si-based photoanodes modified with SLG or its derivatives.^[9b,24] The PEC OER activity is also among the so far best Ni-based n-Si photoanodes in lit (Table S1, Supporting Information), demonstrating the feasibility of our proposed surface modification strategy by engineering the SLG interlayer. The dark current was measured to be close to zero over the potential applied in

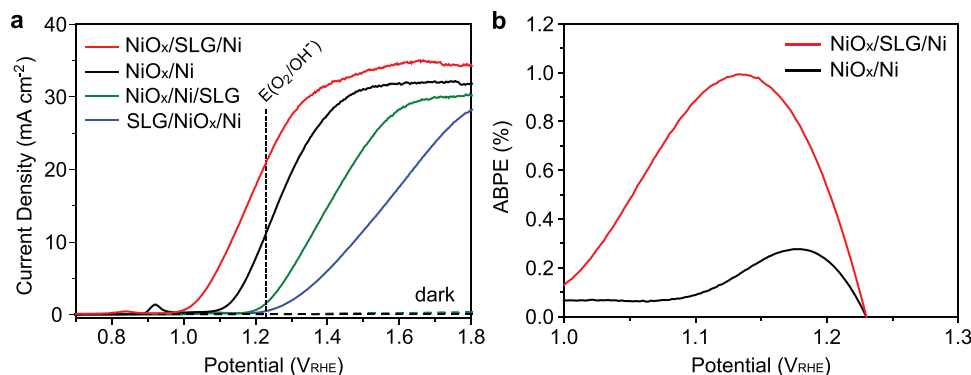


Figure 3. a) J - V curves of the n-Si/TiO₂/NiO_x/SLG/Ni photoanode, with the three n-Si/TiO₂/NiO_x/Ni, n-Si/TiO₂/NiO_x/Ni/SLG, and n-Si/TiO₂/SLG/NiO_x/Ni control samples; b) The ABPE of the n-Si/TiO₂/NiO_x/SLG/Ni photoanode with the SLG-free n-Si/TiO₂/NiO_x/Ni for comparison.

our study, implying that the observed current under irradiation is related to the photogenerated charge carriers. In addition, the n-Si/TiO₂/NiO_x/SLG/Ni photoanode achieves a maximum applied bias photon-to-current efficiency (ABPE) of 1.0% at 1.14 V_{RHE} (Figure 3b), which is ≈ 3.5 times as large as that (0.28% at 1.18 V_{RHE}) of the SLG-free n-Si/TiO₂/NiO_x/Ni control.

To unveil the mechanism of the elevated PEC OER activity of the n-Si/TiO₂/NiO_x/SLG/Ni photoanode compared with the SLG-free n-Si/TiO₂/NiO_x/Ni as a comparison, we first investigated their photovoltage property. The photovoltage here is defined as the difference between the voltage measured at a current of 1 mA cm⁻² for the photoelectrodes under irradiation and the one for the metallic p⁺-Si systems in the dark.^[25] The photo-

voltage of 530 mV is achieved for the n-Si/TiO₂/NiO_x/SLG/Ni, which is higher than that (510 mV) of the n-Si/TiO₂/NiO_x/Ni (Figure 4a), and is also among the reported highest values for Ni-based n-Si photoanodes (Table S1, Supporting Information). This high photovoltage might be attributed to passivation of the Si surface states by TiO₂, the ion-permeable property and/or the high work function of the outer Ni layer influenced by the SLG interlayer (Figure S5, Supporting Information).^[12,18b,26] In principle, the photovoltage in a photoelectrode is determined by the surface barrier height of the semiconductor.^[27] To further clarify the increased photovoltage in the n-Si/TiO₂/NiO_x/SLG/Ni photoanode, we calculate its barrier height through the flat-band potential measured from Mott-Schottky plots. Figure 4b

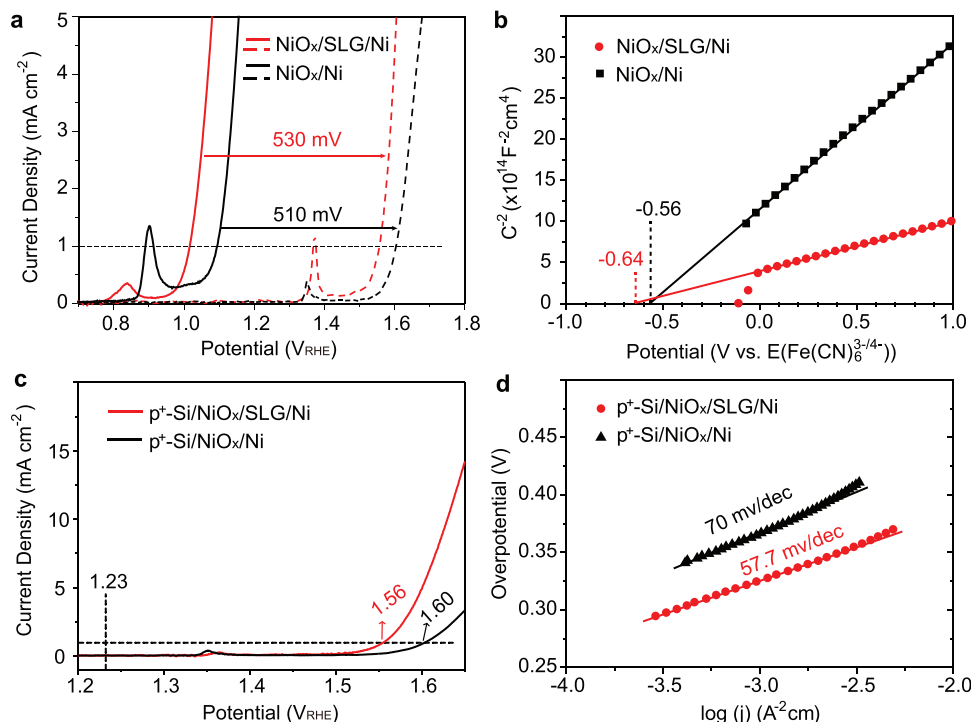


Figure 4. a) Representative J - V plots for the n-Si/TiO₂/NiO_x/SLG/Ni and n-Si/TiO₂/NiO_x/Ni samples in the light (the solid lines) compared to the p⁺-Si/NiO_x/SLG/Ni and the p⁺-Si/NiO_x/Ni in the dark (the dashed lines). b) Mott-Schottky plots of the inverse square space charge capacitance as a function of applied voltage relative to the redox potential of Fe(CN)₆^{3-/4-} for the n-Si/TiO₂/NiO_x/Ni and n-Si/TiO₂/NiO_x/SLG/Ni photoanodes. c) The J - V and d) Tafel plots of the p⁺-Si/NiO_x/SLG/Ni and p⁺-Si/NiO_x/Ni samples in 1 M KOH with 5 mV s⁻¹ scan rate.

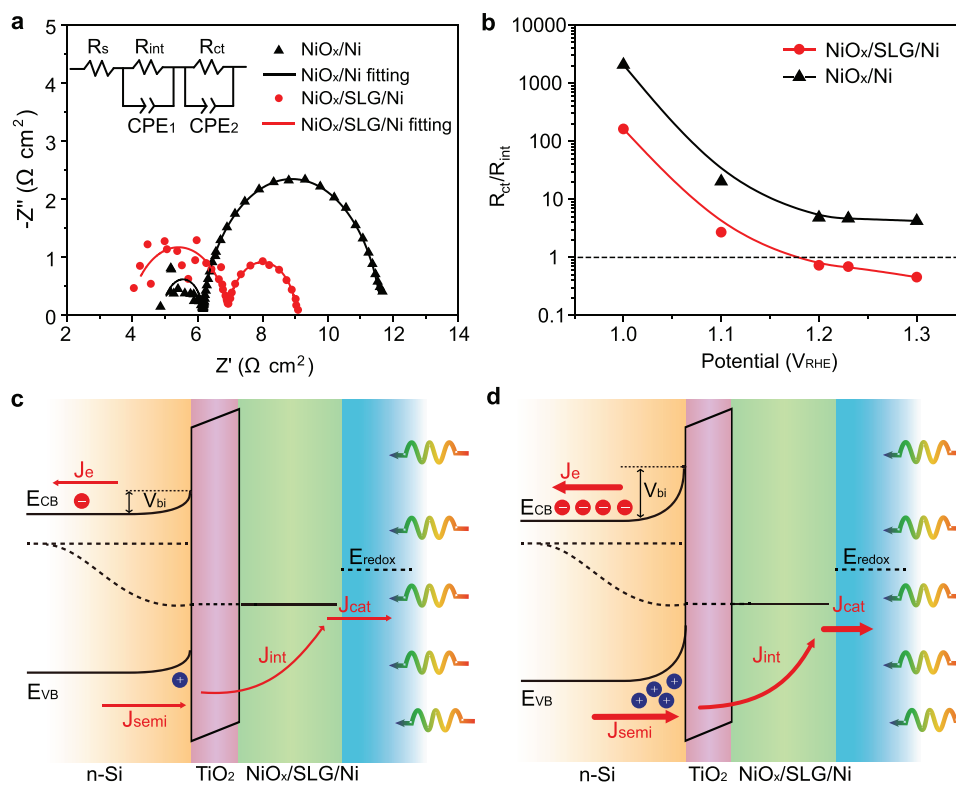


Figure 5. a) Typical Nyquist plots of the n-Si/ TiO_2 / NiO_x /SLG/Ni and n-Si/ TiO_2 / NiO_x /Ni photoanodes measured at 1.23 V_{RHE} , and inset shows the equivalent circuit. b) Variation of the ratio of $R_{\text{ct}}/R_{\text{int}}$ with applied potentials for the n-Si/ TiO_2 / NiO_x /SLG/Ni and n-Si/ TiO_2 / NiO_x /Ni photoanodes. Schematic illustration of charge transfer processes in the n-Si/ TiO_2 / NiO_x /SLG/Ni photoanode for the PEC OER c) at low biases and d) at high biases. E_{CB} , E_{VB} , and E_{redox} represent for the energy level of the conduction band minimum and the valence band maximum of the n-Si, and the redox energy level of the electrolyte, respectively. The red arrow line thickness indicates the relative charge transfer intensity.

exhibits a more negative flat-band potential of -0.64 V versus $E(\text{Fe}(\text{CN})_6^{3-/4-})$ for the n-Si/ TiO_2 / NiO_x /SLG/Ni compared to -0.56 V versus $E(\text{Fe}(\text{CN})_6^{3-/4-})$ for the n-Si/ TiO_2 / NiO_x /Ni, corresponding to a barrier height of 0.84 eV, and this value is higher than that of 0.76 eV of the n-Si/ TiO_2 / NiO_x /Ni (see Experimental section for the calculation method), which is consistent with the higher photovoltage observed in the n-Si/ TiO_2 / NiO_x /SLG/Ni photoanode than that of the n-Si/ TiO_2 / NiO_x /Ni.

We next compared the electrocatalytic OER activity of the NiO_x /SLG/Ni structure with that of the NiO_x /Ni control. Representative OER currents of the samples were measured on the highly conductive ($0.001\text{--}0.005 \Omega \text{ cm}$) p^+ -Si electrode in 1 M KOH aqueous electrolyte. As shown in Figure 4c, the p^+ -Si/ NiO_x /SLG/Ni sample requires an OER overpotential of 330 mV at 1 mA cm^{-2} , which is 40 mV lower than that of the p^+ -Si/ NiO_x /Ni. Moreover, the Tafel slope (57.7 mV dec^{-1}) of the p^+ -Si/ NiO_x /SLG/Ni is smaller than that (70 mV dec^{-1}) of the p^+ -Si/ NiO_x /Ni sample (Figure 4d). The above observations demonstrate the superior electrocatalytic OER activity of the NiO_x /SLG/Ni sandwich structure relative to the NiO_x /Ni reference,^[18b] which is attributed to the SLG's role in improving the catalytic activity of the catalyst by increasing the specific surface area and tuning the electronic structure of the catalyst.^[14b,28] Taken together, the NiO_x /SLG/Ni sandwich structure provides a high photovoltage in the n-Si photoanode and accelerates the OER kinetics as compared to the NiO_x /Ni counterpart.

Then photoelectrochemical impedance spectroscopy (PEIS) was used to investigate charge transfer resistances in the bulk photoanode as well as at the photoanode/electrolyte interface. Typical PEIS spectra at 1.23 V_{RHE} (Figure 5a) show two semi-circles, which are assigned to the charge transfer process at the interface junction of the Si/surface modification layer and at the photoanode/electrolyte interface, respectively, and can be modeled to the equivalent circuit shown in Figure 5a inset.^[24,29] The n-Si/ TiO_2 / NiO_x /SLG/Ni photoanode exhibits a larger average junction resistance (denoted as R_{int}) ($3.13 \Omega \text{ cm}^2$) than the n-Si/ TiO_2 / NiO_x /Ni ($1.28 \Omega \text{ cm}^2$). The larger R_{int} for the n-Si/ TiO_2 / NiO_x /SLG/Ni photoanode can be due to the weak interaction nature (physical contact) between the inner NiO_x and SLG as compared to the strong chemical interaction between the NiO_x and Ni in the n-Si/ TiO_2 / NiO_x /Ni sample.^[30] By contrast, the significantly smaller charge transfer resistance at the photoanode/electrolyte interface (denoted as R_{ct}) for the n-Si/ TiO_2 / NiO_x /SLG/Ni as compared to that of the n-Si/ TiO_2 / NiO_x /Ni is well in line with the boosted OER kinetics for the NiO_x /SLG/Ni structure during the electrocatalytic OER process.

In principle, the total photohole current of the PEC OER is determined by three components including the photohole current from the bulk to the surface in the semiconductor (J_{semi}), the photohole transfer current from the semiconductor surface to the electrocatalyst surface (J_{int}), and the photohole injection current from the electrocatalyst surface to the electrolyte

$(J_{\text{cat}})^{[31]}$ J_{semi} relies on the space charge region governing by the photovoltage (V_{ph}); J_{int} is related to charge transfer resistance at both semiconductor/interlayer and interlayer/electrocatalyst interfaces; and J_{cat} depends on the electrocatalytic activity of the electrocatalyst. Here, the $R_{\text{ct}}/R_{\text{int}}$ value is used to ascertain the limiting step in the transfer process of the photoholes to the electrolyte (the PEIS spectra and the fitting results at different biases can be found in Figure S7 and Table S2, Supporting Information). As seen from the curves in Figure 5b, at low biases (1.0–1.1 V_{RHE}), the hole transfer at the photoanode/electrolyte interface is the limiting step for both n-Si/TiO₂/NiO_x/SLG/Ni and n-Si/TiO₂/NiO_x/Ni photoanodes. This can be understood by the low photohole concentration on the photoanode surface mainly due to the small J_{semi} at low biases (Figure 5c; Figure S8a, Supporting Information). At high biases (1.2–1.3 V_{RHE}), the increased barrier height (V_{bi}) leads to higher J_{semi} values in both photoanodes and thus enough photoholes can reach the photoanode surface (see Figure 5d; Figure S8b, Supporting Information). Meanwhile, the photoelectron current (J_{e}) to the counter electrode also increases due to the larger V_{bi} compared to that at low biases. In such case, the hole transfer at the photoanode/electrolyte interface is still the limiting step for the n-Si/TiO₂/NiO_x/Ni sample, which is the result of its lower J_{cat} but higher J_{int} (Figure S8b, Supporting Information). In contrast, for the n-Si/TiO₂/NiO_x/SLG/Ni sample, because of its larger J_{cat} and relatively lower J_{int} , photoholes reaching the photoanode surface can inject to the electrolyte efficiently and hole transfer in the solid junction becomes the limiting

step (Figure 5d). In aligned with the above Raman analysis, the Ni is chemisorbed on the SLG interlayer, ensuring a good interface quality, and hence benefits for the interfacial charge transfer between the SLG and Ni layer. The red shift in G peak as well as the blue shift in 2D peak for the SiO₂/NiO_x/SLG as compared to the SiO₂/SLG (Figure S4, Supporting Information) is observed due to the hole doping of the SLG by the charge transfer between the NiO_x and SLG,^[32] which indicates that the interface quality for charge transfer between the NiO_x and SLG is also high. Therefore, the photohole transfer in the n-Si/TiO₂/NiO_x/SLG/Ni photoanode is still effective owing to the excellent electronic contact between the inner NiO_x and SLG, although it possesses a lower J_{int} as compared to the n-Si/TiO₂/NiO_x/Ni control. Most importantly, a synergistic regulation on J_{semi} , J_{int} , and J_{cat} in the n-Si/TiO₂/NiO_x/SLG/Ni photoanode is achieved via designing the sandwich structure with the SLG as the interlayer, leading to the optimized total hole current and thus the boosted PEC OER activity.

Charge transfer behavior in the n-Si/TiO₂/NiO_x/SLG/Ni photoanode was further exploited by transient photocurrent measurements. The photocurrent spikes are typically observed during the transient state when the light is switched on/off. A sharp photocurrent spike is attributed to the recombination of accumulated photogenerated holes at the photoanode/electrolyte interface because of the slow OER kinetics. In comparison with the n-Si/TiO₂/NiO_x/Ni, the n-Si/TiO₂/NiO_x/SLG/Ni photoanode has a weak spike current (Figure 6a), indicating an excellent interface quality with reduced charge recombination. The

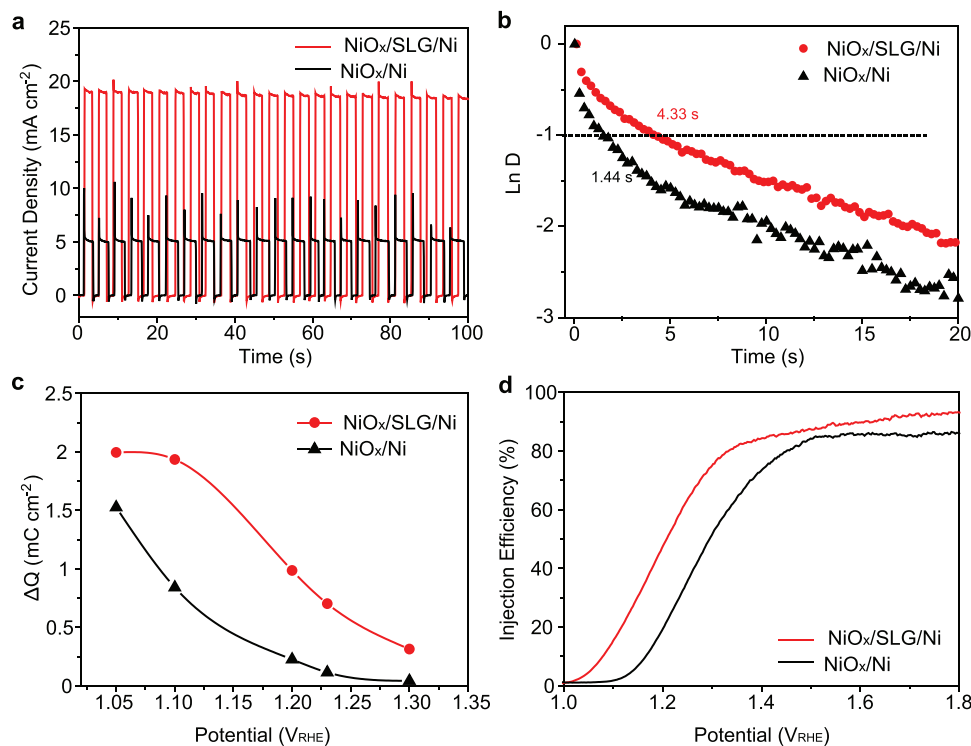


Figure 6. a) The transient photocurrent curves of the n-Si/TiO₂/NiO_x/SLG/Ni and n-Si/TiO₂/NiO_x/Ni photoanodes measured at an applied bias of 1.23 V_{RHE} . b) The correlation between $\ln D$ and time, and the transient time constant is defined as the time when $\ln D = -1$. c) Charge storage density versus potential curves of the n-Si/TiO₂/NiO_x/SLG/Ni and n-Si/TiO₂/NiO_x/Ni photoanodes. d) Charge injection efficiencies for the n-Si/TiO₂/NiO_x/SLG/Ni and n-Si/TiO₂/NiO_x/Ni photoanodes.

charge recombination behavior can be quantitatively reflected by the transient time constant τ , which is defined as the time when $\ln D = -1$ (Figure 6b; Figure S9, Supporting Information).^[29] The τ values of the n-Si/TiO₂/NiO_x/SLG/Ni and n-Si/TiO₂/NiO_x/Ni photoanodes are extracted to be ≈ 4.33 and 1.44 s, respectively. The higher τ represents the lower interfacial charge recombination, implying that the SLG layer in the n-Si/TiO₂/NiO_x/SLG/Ni photoanode decreases the recombination of photogenerated electrons and holes at the photoanode-electrolyte interface. According to the previous work,^[33] a high surface hole concentration is beneficial for the hole transfer at the photoanode/electrolyte interface. The amount of hole storage is then qualitatively determined by the transient cathodic current (Figure S10, Supporting Information). As shown in Figure 6c, the n-Si/TiO₂/NiO_x/SLG/Ni photoanode has much larger hole storage density than the n-Si/TiO₂/NiO_x/Ni during the OER process, which is attributed to the superb charge trap and storage ability of the SLG,^[34] ensuring that enough holes can survive on the photoanode surface for the OER instead of recombination. As a result, the interfacial hole transfer in the n-Si/TiO₂/NiO_x/SLG/Ni photoanode is more kinetically favorable as compared to that in the n-Si/TiO₂/NiO_x/Ni. This can be further corroborated by comparing their charge injection efficiencies. Figure 6d displays that the n-Si/TiO₂/NiO_x/SLG/Ni photoanode has a higher charge injection efficiency than the n-Si/TiO₂/NiO_x/Ni at a potential larger than 1.0 V_{RHE}, and reaches up to > 90% when the potential is larger than 1.6 V_{RHE}. Combining the above analysis, such a high injection efficiency of the n-Si/TiO₂/NiO_x/SLG/Ni photoanode is put down to the high surface hole concentration thanks to both the high hole storage ability and the fast interfacial hole transfer of the engineered SLG interfaces.

Additionally, the stability test shows the photocurrent of the n-Si/TiO₂/NiO_x/SLG/Ni photoanode can be stable for 2 h and maintain at 89% of the initial photocurrent after 3 h operation at a constant bias of 1.8 V_{RHE} (Figure S11a, Supporting Information). The SEM image of the sample subjected to the 3 h stability test indicates that parts of the SLG/Ni layer peel off from the n-Si/TiO₂/NiO_x substrate, leaving a broken SLG sheet on the photoanode surface (Figure S11b, Supporting Information). Thus, the detachment of the surface SLG/Ni layer decreases the photocurrent, which could be attributed to the weak interaction between the SLG and NiO_x layers.

Finally, to check the generality of the strategy for engineering the SLG in the form of sandwich structure for the lifted PEC OER activity, we replaced metal Ni with Co and Fe and accordingly constructed the FeO_x/SLG/Fe, NiO_x/SLG/Fe, CoO_x/SLG/Co, NiO_x/SLG/Co sandwich structures on the n-Si substrate. As exhibited in Figure S12 (Supporting Information), all of the SLG-interlayered sandwich structures modified n-Si photoanodes bolster the PEC OER activity as compared to their corresponding counterparts.

By replacing the MO_x layer with other materials with higher work functions like Pt, substituting the M layer with other electrocatalysts, or tightening the interfacial interaction in our MO_x/SLG/M sandwich structure, a better PEC OER activity is expected. Further improvement on the stability of the photoanodes could also be expected by strengthening the SLG/substrate interaction, for instance, by direct growth of the SLG layer on

the MO_x layer, or by deposition of the SLG-based sandwich structure onto the semiconductor substrate with nano/micro-textures.^[35] With the rapid development of graphene growth techniques, there is no problem that this issue will be well addressed in the future.

3. Conclusion

In summary, we have proposed and developed a novel transition metal oxide/SLG/metal sandwich structure to engineer the n-Si-based photoanode for improved PEC OER activity. It is attributed to the key roles of the SLG interlayer in the form of sandwich configuration: 1) obtaining the high photovoltage owing to modulation of the morphology, structure, and work function of the surface metal electrocatalyst; 2) accelerating surface reaction kinetics as an effective support for the electrocatalyst, and further promoting the photohole injection for the OER out of the high charge trap and storage ability; and 3) synergistically tailoring the three photohole involved currents of the material in the bulk, at the interface and on the catalyst surface for the enhanced PEC OER. Our findings suggest that SLG can be an effective interface layer by rational structural design in the PEC cell to promote its solar water-splitting performance, which could also be applied to other systems for higher solar energy conversion.

4. Experimental Section

Materials: The moderately phosphorous-doped n-type crystalline Si (100) wafers with a thickness of 500 ± 10 μm and a resistivity of 0.1–0.9 Ω cm (n-Si) were purchased from Zhejiang Lijing Guangdong Technology Co., Ltd. Single-layer graphene with a coverage of > 99% on a 25 μm thick copper foil was supplied by Chongqing Graphene Technology Co., Ltd. Metallic Ni wire (99.9%), metallic Fe pellet (99.95%), and metallic Co pellet (99.95%) were purchased from Zhongnuo New Material Co., Ltd.

Preparation of the Photoanodes: First, the n-Si wafer was cut into ≈ 1 cm \times 1 cm pieces and cleaned in an ultrasonic bath of acetone, isopropanol, and ethanol sequentially. Then the pieces were dipped into a 2% HF solution for 2 min to remove the native oxide, followed by rinsing with deionized water and drying with flowing N₂ (step i). Next, a 2 nm thick passivation tunneling TiO₂ layer was immediately deposited on the n-Si substrates using ALD (step ii). After that, 2 nm thick metallic Ni thin film was thermally evaporated onto the TiO₂ layer (step iii). A SLG layer was then transferred onto the substrate by a PMMA assisted method. Subsequently, the sample was baked at 300 $^{\circ}\text{C}$ for 10 min to transform the metallic Ni layer to NiO_x as well as to strengthen the adhesion between the SLG and the substrate (step iv). Finally, another metallic Ni thin film with 2 nm thickness was deposited onto the SLG to form the NiO_x/SLG/Ni sandwich structure on the photoanode (step v).

Analogous procedures were used to fabricate photoanodes with other SLG-based structures (n-Si/SLG/NiO_x/Ni and n-Si/NiO_x/Ni/SLG) and without SLG (n-Si/NiO_x/Ni). For the fabrication of n-Si/SLG/NiO_x/Ni and n-Si/NiO_x/Ni/SLG, the above step (iv) was processed before the step (iii) and after the step (v), respectively. During the n-Si/NiO_x/Ni fabrication, the samples were also processed by exposing them to the same conditions as the SLG transfer procedure, except that no SLG was present between the PMMA and Cu. The same NiO_x/Ni and NiO_x/SLG/Ni structure were also deposited on the p⁺-Si and quartz substrates to examine their electrochemical and optical transmittance properties, respectively. In addition, n-Si/FeO_x/Fe, n-Si/FeO_x/SLG/Fe, n-Si/CoO_x/Co, n-Si/CoO_x/SLG/Co, n-Si/NiO_x/Fe, n-Si/NiO_x/SLG/Fe, n-Si/NiO_x/Co,

and n-Si/NiO_x/SLG/Co photoanodes were also fabricated using the same process as described above, except that the metallic Ni target for thermal evaporation was replaced by the corresponding metallic Fe or Co target.

To fabricate the electrode for PEC measurements, the ohmic contact was done on the backside of the n-Si sample by scratching the surface with a diamond glass cutter to remove the oxide layer, followed by cleaning the residue using ethanol; then a droplet of InGa alloy and a Cu wire was applied on the scratched part, and the backside and frontside of the surface except an active area of 0.1–0.2 cm² were shielded by use of black 704 silicone rubber. Calibrated digital images and Image J software were employed to measure the exact geometric area of the active electrode surface.

ALD Growth of TiO₂: The TiO₂ layer was deposited at 200 °C using successive pulses of tetrakis (dimethylamido) titanium (75 °C) and H₂O (room temperature), respectively, as the titanium source and oxidant under a N₂ carrier gas in a vacuum chamber using an ALD system (TALD-100A, KE-MICRO). During the deposition, the base pressure of the ALD chamber was between 190 and 200 mTorr. In a typical process, one ALD cycle consists of tetrakis (dimethylamido) titanium dose for 0.2 s, N₂ purge for 40 s, H₂O dose for 0.2 s, and N₂ purge for 40 s. Spectroscopic ellipsometry measurement indicates a TiO₂ growth rate of 0.04 nm per cycle, and 60 cycles of ALD were performed to deposit the TiO₂ with a thickness of ≈2.4 nm.

Thermal Evaporation of Ni Thin Film: A thermal evaporator (ZHD-300, Techno) was used to prepare the Ni thin film. The base pressure of the vacuum chamber of this system was ≈5 × 10⁻⁴ Pa. During the evaporation process, the current and voltage on a tungsten boat containing the Ni wire target were monitored in order to establish the vapor pressure in the chamber needed to maintain a constant evaporation rate of 1 Å s⁻¹, and the film thickness was controlled using quartz crystal thickness monitor.

PMMA Assisted Transfer of Graphene: The copper foil (Cu) with SLG was cut into a proper size (≈0.6 cm × 0.6 cm). Next, the SLG/Cu was spin-coated (1,000 rpm for 20 s, then 4,000 rpm for 30 s) with a PMMA solution (4 wt.% dissolved in anisole), which was then cured at 120 °C for 2 min. Subsequently, the PMMA/SLG/Cu was floated in a 1 M FeCl₃ + 1 M HCl solution over a period of ≈12 h to remove the Cu. Afterward, the PMMA/SLG film was thoroughly rinsed with deionized water three times to eliminate the remaining etchant, and placed on the target substrates and dried naturally. After baking under 120 °C for 10 min, the sample was first immersed in an acetone bath for 1 h then in a warm acetone bath under 50 °C for 2 h, and was subsequently dipped into isopropyl alcohol for another 1 h to remove the PMMA film. Finally, the sample covered with SLG was obtained after drying with flowing N₂.

Characterizations: The morphology of the samples was examined by a Hitachi-SU8220 field emission scanning electron microscopy (SEM) at an accelerating voltage of 10 KV. Raman spectra were collected on a Renishaw InVia Plus laser Raman spectrometer at room temperature using the 514 nm line of an Ar⁺-ion laser as the excitation source. XPS was conducted with an ESCALAB250Xi using 300 W Al Kα radiation; the base pressure was ≈3 × 10⁻⁹ mbar. Binding energies were referenced to the C 1s line at 284.8 eV from adventitious carbon. XPS spectra were analyzed using the XPSPEAK41 software. The background was removed using a Shirley-type background and the spectra were fitted using Gaussian–Lorentzian peaks (80% of Gaussian character). The ultraviolet photoelectron spectroscopy (UPS) was collected using He I discharge lamp (hν = 21.22 eV) as an excitation source, and the value of work function was measured from the secondary-electron cut-off using a gold metal reference. Reflectance and transmittance spectra were recorded using a UV-2600 UV–vis spectrophotometer (Shimadzu, Japan) equipped with an integrating sphere. Reflectance spectra of the photoanodes were measured at near-normal incidence (θ = 8°) in air. And the transmittance property of the surface modification layer was examined by collecting the transmittance spectra of the surface modification layer deposited on the quartz substrate at normal incidence in air.

Photoelectrochemical Measurements: All PEC measurements were performed on a Zahner–Zennium electrochemical workstation at room

temperature under a three-electrode configuration with a saturated calomel electrode (SCE) and a Pt foil as the reference electrode and the counter electrode, respectively. The as-prepared photoanodes were set as the working electrode, and a 1 M KOH aqueous solution (pH 13.62 measured by a pH meter) was used as the electrolyte. A 500 W xenon lamp (Beijing Aulight Technology Co., Ltd.; CEL-S500) equipped with an AM 1.5G filter was used as the light source, and the light intensity was calibrated to be one sun (100 mW cm⁻²) at the position of the photoanodes using a fiber optic spectrometer (Avantes, Netherland; AvaSpec-ULS2048). All measured potentials were converted to the reversible hydrogen electrode (RHE) reference using the following equation: V_{RHE} = V_{SCE} + 0.244 V + 0.059 pH, where V_{SCE} is the measured potential against SCE reference electrode. All reported potentials were intentionally not corrected by the Ohmic drop (i.e., no *iR* correction). The photocurrent was recorded by linear sweep voltammetry with a scan rate of 20 mV s⁻¹, and the chronoamperometric data were collected at a constant potential of 1.8 V_{RHE}. The PEIS was conducted under light irradiation conditions at series potentials of 1.0–1.3 V_{RHE} for the sweeping frequency range from 100 kHz to 0.1 Hz with an AC amplitude of 5 mV. The PEIS data were fit to the equivalent circuit that was discussed in the text, using the Zview software. Mott–Schottky measurements were performed under dark conditions using a Pt foil counter electrode and a Pt wire reference electrode in 50 mM K₃Fe(CN)₆, 350 mM K₄Fe(CN)₆, and 1 M KCl. During the measurement, the potential was swept from positive to negative values with a frequency of 7000 Hz and an AC amplitude of 5 mV.

The charge injection efficiency (η_{inj}) of the photoanode was determined as the following equation by adding 0.5 M H₂O₂ to the KOH electrolyte to suppress the surface recombination of the charge carriers without influencing the charge separation in the electrode bulk.

$$\eta_{inj} = J_{H_2O} / J_{H_2O_2} \quad (1)$$

where J_{H₂O} and J_{H₂O₂} are the photocurrent densities for PEC H₂O oxidation and H₂O₂ oxidation, respectively.

The barrier height (φ_b) at the n-Si and surface modification layer interface was calculated using the Schottky's relation:

$$\phi_b = E_{fb} + V_n \quad (2)$$

where E_{fb} is the flat-band potential and V_n is the potential difference between the Fermi level and the conduction band edge of n-Si.

E_{fb} is determined from Mott–Schottky measurements according to the Mott–Schottky relation:

$$\frac{1}{C^2} = \frac{2}{A\epsilon_0\epsilon_r q N_d} \left(V - E_{fb} - \frac{kT}{q} \right) \quad (3)$$

where C is the capacitance of the space charge region in the n-Si semiconductor, ε₀ is the vacuum permittivity (8.85 × 10⁻¹² F m⁻¹), ε_r is the relative permittivity of Si (11.7), A is the area of the photoanode, q is the elementary charge (1.6 × 10⁻¹⁹ C), k is the Boltzmann's constant (1.38 × 10⁻²³ J K⁻¹), T is the temperature (300 K), V is the applied bias, and N_d is the donor concentration of the n-Si. The E_{fb} was obtained by taking the value of the intercept between the extrapolated linear region of the C⁻² with the x-axis in the Mott–Schottky plot.

And V_n was determined following the equation:

$$V_n = \frac{kT}{q} \ln(N_c / N_d) \quad (4)$$

The effective density of states in the conduction band (N_c) of n-Si was calculated following the equation

$$N_c = 2 \left(\frac{2\pi m_e^* kT}{h^2} \right)^{3/2} \quad (5)$$

where m_e^* is the electron effective mass of n-Si ($1.09m_e$ at 300 K, $m_e = 9.109 \times 10^{-31}$ Kg is the electron rest mass). Then the calculated N_c value was $2.82 \times 10^{25} \text{ m}^{-3}$. And the N_d of n-Si was calculated to be $1.04 \times 10^{22} \text{ m}^{-3}$ from the equation $N_d = 1/q\mu\rho$, where μ is the electron mobility ($531 \text{ cm}^2 \text{ V}^{-1} \text{ s}^{-1}$), and ρ is the resistivity ($0.5 \text{ } \Omega \text{ cm}$). From the calculated N_c and N_d , V_n was thus calculated to be 0.2 eV.

Supporting Information

Supporting Information is available from the Wiley Online Library or from the author.

Acknowledgements

The authors acknowledge financial support for this work from the Strategic Priority Research Program of CAS (XDB36000000) and National Natural Science Foundation of China (22102037, 22179028, and 22002028).

Conflict of Interest

The authors declare no conflict of interest.

Data Availability Statement

The data that support the findings of this study are available in the supplementary material of this article.

Keywords

interfacial charge transfers, photoelectrochemical water oxidation, photovoltages, single-layer graphenes

Received: September 7, 2022

Revised: October 27, 2022

Published online:

- [1] a) D. Chen, H. Zhang, Y. Liu, J. Li, *Energy Environ. Sci.* **2013**, *6*, 1362; b) C. Li, Q. Cao, F. Wang, Y. Xiao, Y. Li, J.-J. Delaunay, H. Zhu, *Chem. Soc. Rev.* **2018**, *47*, 4981; c) B. Koo, S. Byun, S.-W. Nam, S.-Y. Moon, S. Kim, J. Y. Park, B. T. Ahn, B. Shin, *Adv. Func. Mater.* **2018**, *28*, 1705136; d) Y. Hou, Z. Wen, S. Cui, X. Guo, J. Chen, *Adv. Mater.* **2013**, *25*, 6291; e) F. Ning, M. Shao, S. Xu, Y. Fu, R. Zhang, M. Wei, D. G. Evans, X. Duan, *Energy Environ. Sci.* **2016**, *9*, 2633.
- [2] Z. Long, X. Tong, C. Liu, A. I. Channa, R. Wang, X. Li, F. Lin, A. Vomiero, Z. M. Wang, *Chem. Eng. J.* **2021**, *426*, 131298.
- [3] a) U. Sim, J. Moon, J. An, J. H. Kang, S. E. Jerng, J. Moon, S.-P. Cho, B. H. Hong, K. T. Nam, *Energy Environ. Sci.* **2015**, *8*, 1329; b) U. Sim, T.-Y. Yang, J. Moon, J. An, J. Hwang, J.-H. Seo, J. Lee, K. Y. Kim, J. Lee, S. Han, B. H. Hong, K. T. Nam, *Energy Environ. Sci.* **2013**, *6*, 3658.
- [4] a) Y. Wang, L. Wang, H.-Y. Wang, Q.-D. Chen, H.-B. Sun, *J. Phys. Chem. C* **2019**, *123*, 22550; b) F. Joucken, L. Henrard, J. Lagoute, *Phys. Rev. Mater.* **2019**, *3*, 110301.
- [5] a) G. Xie, K. Zhang, H. Fang, B. Guo, R. Wang, H. Yan, L. Fang, J. R. Gong, *Chem. Asian J.* **2013**, *8*, 2395; b) A. K. Alves, A. C. S. Frantz, F. A. Berutti, *Flat. Chem.* **2018**, *12*, 26.
- [6] F. Liu, P. Li, H. An, P. Peng, B. McLean, F. Ding, *Adv. Func. Mater.* **2022**, *32*, 2203191.
- [7] Y. Chen, B. Zhang, G. Liu, X. Zhuang, E.-T. Kang, *Chem. Soc. Rev.* **2012**, *41*, 4688.
- [8] a) A. C. Nielander, M. J. Bierman, N. Petrone, N. C. Strandwitz, S. Ardo, F. Yang, J. Hone, N. S. Lewis, *J. Am. Chem. Soc.* **2013**, *135*, 17246; b) A. C. Nielander, A. C. Thompson, C. W. Roske, J. A. Maslyn, Y. Hao, N. T. Plymale, J. Hone, N. S. Lewis, *Nano Lett.* **2016**, *16*, 4082.
- [9] a) C. K. Ku, P. H. Wu, C. C. Chung, C. C. Chen, K. J. Tsai, H. M. Chen, Y. C. Chang, C. H. Chuang, C. Y. Wei, C. Y. Wen, *Adv. Energy Mater.* **2019**, 1901022; b) K. Yoon, J.-H. Lee, J. Kang, J. Kang, M. J. Moody, M. C. Hersam, L. J. Lauhon, *Nano Lett.* **2016**, *16*, 7370; c) S. E. Jun, S. Choi, S. Choi, T. H. Lee, C. Kim, J. W. Yang, W.-O. Choe, I.-H. Im, C.-J. Kim, H. W. Jang, *Nano-Micro Lett.* **2021**, *13*, 81.
- [10] a) U. Sim, J. Moon, J. Lee, J. An, H.-Y. Ahn, D. J. Kim, I. Jo, C. Jeon, S. Han, B. H. Hong, K. T. Nam, *ACS Appl. Mater. Interfaces* **2017**, *9*, 3570; b) S. A. Carminati, A. do Nascimento Barbosa, A. L. M. de Freitas, F. L. Freire Jr, F. L. Souza, A. F. Nogueira, *J. Catal.* **2019**, *372*, 109; c) Q. Qin, Q. Cai, W. Hong, C. Jian, W. Liu, *Chem. Eng. J.* **2020**, *402*, 126227.
- [11] a) G. Xie, S. U. Jan, Z. Dong, Y. Dai, R. Boddula, Y. Wei, C. Zhao, Q. Xin, J.-N. Wang, Y. Du, L. Ma, B. Guo, J. R. Gong, *Chin. J. Catal.* **2020**, *41*, 2; b) Z. Yin, Y. Shi, S. Shen, *Sci. Chin. Mater.* **2022**; c) S. Lee, L. Ji, A. C. De Palma, E. T. Yu, *Nat. Commun.* **2021**, *12*, 3982.
- [12] I. A. Digdaya, G. W. P. Adhyaksa, B. J. Trzeźniewski, E. C. Garnett, W. A. Smith, *Nat. Commun.* **2017**, *8*, 15968.
- [13] G. Xie, K. Zhang, B. Guo, Q. Liu, L. Fang, J. R. Gong, *Adv. Mater.* **2013**, *25*, 3820.
- [14] a) J. Zhang, Q. Zhang, X. Feng, *Adv. Mater.* **2019**, *31*, 1808167; b) C. Wang, D. Astruc, *Prog. Mater. Sci.* **2018**, *94*, 306.
- [15] T. Yao, R. Chen, J. Li, J. Han, W. Qin, H. Wang, J. Shi, F. Fan, C. Li, *J. Am. Chem. Soc.* **2016**, *138*, 13664.
- [16] L. De Los Santos Valladares, A. Ionescu, S. Holmes, C. H. Barnes, A. Bustamante Domínguez, O. Avalos Quispe, J. C. González, S. Milana, M. Barbone, A. C. Ferrari, *J. Vac. Sci. Technol. B* **2014**, *32*, 051808.
- [17] a) F. Ruffino, F. Giannazzo, *Crystals* **2017**, *7*, 219; b) X. Liu, Y. Han, J. W. Evans, A. K. Engstfeld, R. J. Behm, M. C. Tringides, M. Hupalo, H.-Q. Lin, L. Huang, K.-M. Ho, *Prog. Surf. Sci.* **2015**, *90*, 397.
- [18] a) F. A. L. Laskowski, M. R. Nellist, R. Venkatkarthick, S. W. Boettcher, *Energy Environ. Sci.* **2017**, *10*, 570; b) J. C. Hill, A. T. Landers, J. A. Switzer, *Nat. Mater.* **2015**, *14*, 1150; c) F. Lin, S. W. Boettcher, *Nat. Mater.* **2014**, *13*, 81.
- [19] a) C. Pan, R. Zhang, R. G. Nuzzo, A. A. Gewirth, *Adv. Energy Mater.* **2018**, *8*, 1800589; b) L. Ye, Y. Zhou, Z. Bao, Y. Zhao, Y. Zou, L. Zhao, Q. Jiang, *J. Mater. Chem. A* **2018**, *6*, 19020; c) S. Xu, T. Wang, Y. Ma, W. Jiang, S. Wang, M. Hong, N. Hu, Y. Su, Y. Zhang, Z. Yang, *ChemSusChem* **2017**, *10*, 4056.
- [20] G. Loget, C. Mériadec, V. Dorcet, B. Fabre, A. Vacher, S. Fryars, S. Ababou-Girard, *Nat. Commun.* **2019**, *10*, 3522.
- [21] L. Malard, M. Pimenta, G. Dresselhaus, M. Dresselhaus, *Phys. Rep.* **2009**, *473*, 51.
- [22] a) I. Serrano-Esparza, J. Fan, J. M. Michalik, L. A. Rodríguez, M. R. Ibarra, J. M. de Teresa, *J. Phys. D* **2016**, *49*, 105301; b) D. Y. Usachov, V. Y. Davydov, V. S. Levitskii, V. O. Shevelev, D. Marchenko, B. V. Senkovskiy, O. Y. Vilkov, A. G. Rybkin, L. V. Yashina, E. V. Chulkov, *ACS Nano* **2017**, *11*, 6336.
- [23] a) A. J. Shih, N. Arulmozhi, M. T. Koper, *ACS Catal.* **2021**, *11*, 10892; b) K. Hu, T. Ohto, Y. Nagata, M. Wakisaka, Y. Aoki, J.-i. Fujita, Y. Ito, *Nat. Commun.* **2021**, *12*, 203.
- [24] C. Li, Y. Xiao, L. Zhang, Y. Li, J.-J. Delaunay, H. Zhu, *Sustain. Energy Fuels* **2018**, *2*, 663.
- [25] J. Quinn, J. Hemmerling, S. Lincic, *ACS Catal.* **2018**, *8*, 8545.

- [26] a) C. Du, X. Yang, M. T. Mayer, H. Hoyt, J. Xie, G. McMahon, G. Bischooping, D. Wang, *Angew. Chem., Int. Ed.* **2013**, *52*, 12692; b) R. Liu, Z. Zheng, J. Spurgeon, X. Yang, *Energy Environ. Sci.* **2014**, *7*, 2504; c) I. A. Digdaya, B. J. Trzeźniowski, G. W. P. Adhyaksa, E. C. Garnett, W. A. Smith, *J. Phys. Chem. C* **2018**, *122*, 5462.
- [27] M. J. Kenney, M. Gong, Y. Li, J. Z. Wu, J. Feng, M. Lanza, H. Dai, *Science* **2013**, *342*, 836.
- [28] a) J. Kang, J.-S. Yu, B. Han, *J. Phys. Chem. Lett.* **2016**, *7*, 2803; b) W. Qin, X. Li, *J. Phys. Chem. C* **2010**, *114*, 19009.
- [29] Q. Cai, W. Hong, C. Jian, J. Li, W. Liu, *ACS Catal.* **2018**, *8*, 9238.
- [30] B. Bräuer, Y. Vaynzof, W. Zhao, A. Kahn, W. Li, D. R. T. Zahn, C.d.J. Fernández, C. Sangregorio, G. Salvan, *J. Phys. Chem. B* **2009**, *113*, 4565.
- [31] a) J. Zhang, J. Cui, S. Eslava, *Adv. Energy Mater.* **2021**, *11*, 2003111; b) J. R. Hemmerling, A. Mathur, S. Linic, *Acc. Chem. Res.* **2021**, *54*, 2002.
- [32] a) W. Wang, S. Liang, T. Yu, D. Li, Y. Li, X. Han, *J. Appl. Phys.* **2011**, *109*, 07C501; b) A. Das, S. Pisana, B. Chakraborty, S. Piscanec, S. K. Saha, U. V. Waghmare, K. S. Novoselov, H. R. Krishnamurthy, A. K. Geim, A. C. Ferrari, *Nat. Nanotechnol.* **2008**, *3*, 210.
- [33] G. Xie, L. Guan, L. Zhang, B. Guo, A. Batool, Q. Xin, R. Boddula, S. U. Jan, J. R. Gong, *Nano Lett.* **2019**, *19*, 1234.
- [34] a) D. I. Son, T. W. Kim, J. H. Shim, J. H. Jung, D. U. Lee, J. M. Lee, W. I. Park, W. K. Choi, *Nano Lett.* **2010**, *10*, 2441; b) M. Sup Choi, G.-H. Lee, Y.-J. Yu, D.-Y. Lee, S. Hwan Lee, P. Kim, J. Hone, W. Jong Yoo, *Nat. Commun.* **2013**, *4*, 1624; c) M. D. Stoller, C. W. Magnuson, Y. Zhu, S. Murali, J. W. Suk, R. Piner, R. S. Ruoff, *Energy Environ. Sci.* **2011**, *4*, 4685.
- [35] H. Yu, S. Chen, X. Fan, X. Quan, H. Zhao, X. Li, Y. Zhang, *Angew. Chem., Int. Ed.* **2010**, *49*, 5106.